

# PP-PS registration in the reflectivity domain: A waveform-preserving approach

Daniel O Pérez<sup>1\*</sup> , Danilo R Velis<sup>1</sup> 

**Abstract** Joint PP-PS amplitude inversion and attribute analysis require mapping converted PS wave data to the PP time domain so that similar reflectors share the same two-way travel times. This process, known as PP-PS data registration, often results in non-stationary PS data, where wavelet spectral content varies with time and location, affecting subsequent inversion results and necessitating postprocessing to correct these issues. To address this limitation, we propose a PP-PS registration method in the reflectivity domain. The strategy consists of two steps. First, we perform sparse-spike deconvolution on both PP and PS data to transform them into the reflectivity domain, based on the hypothesis that suitable wavelets and sparse-spike reflectivities can be estimated from the data. The sparse-spike solutions are obtained by solving an inverse problem regularized with a sparsity-promoting norm and solved via proximal algorithms. In the second step, we iteratively adjust the sparse-spike PS reflectivity to match its PP counterpart using a smooth, monotonic warping function derived from the  $v_P/v_S$  ratio, represented as a cubic spline with a fixed number of knots. At each iteration, both reflectivities are convolved with a stationary replacement wavelet, and the resulting match is evaluated. Optimizing the knot values leads to a nonlinear, multimodal problem, which we solve using very fast simulated annealing. Unlike conventional methods that operate in the data domain, our approach produces stationary PP and PS seismic data with aligned reflectors in two-way travel time, eliminating waveform distortions and requiring no additional processing. Numerical tests confirm that the method preserves amplitude and outperforms techniques like dynamic time warping, yielding a cleaner spectrum and distortion-free waveforms for reliable interpretation.

**Keywords** PP-PS registration, inversion, velocity, optimization.

## Registración PP-PS en el dominio de la reflectividad: un enfoque que preserva la forma de onda

**Resumen** La inversión conjunta de amplitudes PP-PS y el análisis de atributos requieren mapear los datos convertidos de ondas PS al dominio temporal PP, de modo que los reflectores similares compartan los mismos tiempos de doble recorrido. Este proceso, conocido como registración de datos PP-PS, suele generar datos PS no estacionarios, en los que el contenido espectral de la ondícula varía con el tiempo y la ubicación, afectando los resultados de la inversión y obligando a aplicar un posprocesamiento correctivo. Para abordar esta limitación proponemos un método de registración PP-PS en el dominio de la reflectividad. La estrategia consta de dos pasos: primero realizamos deconvolución de impulsos dispersos (*sparse-spike*) en los datos PP y PS para transformarlos al dominio de la reflectividad, bajo la hipótesis de que es posible estimar ondículas adecuadas y reflectividades *sparse-spike* a partir de los datos. Las soluciones *sparse-spike* se obtienen resolviendo un problema inverso regularizado con una norma promotora de esparsidad y resuelto mediante algoritmos proximales. En el segundo paso ajustamos iterativamente la reflectividad PS *sparse-spike* para que coincida con su contraparte PP utilizando una función de deformación suave y monótonamente creciente derivada de la razón  $v_P/v_S$ , representada como una *cubic spline* con un número fijo de nudos. En cada iteración ambas reflectividades se convolucionan con una ondícula estacionaria de reemplazo y se evalúa la concordancia resultante. La optimización de los valores de los nudos conduce a un problema no lineal y multimodal que resolvemos mediante *very fast simulated annealing*. A diferencia de los métodos convencionales que operan en el dominio de los datos, nuestro enfoque produce registros sísmicos PP y PS estacionarios con reflectores alineados en tiempo de doble recorrido, eliminando distorsiones de forma de onda y sin necesidad de procesamiento adicional. Pruebas numéricas confirman que el método preserva la amplitud y supera a técnicas como el *dynamic time warping*, generando un espectro más limpio y formas de onda libres de distorsión para una interpretación confiable.

**Palabras clave** Registración PP-PS, inversión, velocidad, optimización.

## INTRODUCTION

Multicomponent seismic data provides additional information that enables, among other valuable applications, simultaneous PP and PS amplitude inversion. This is a powerful tool for revealing subtle reservoir details, improving characterization, and increasing confidence in interpretation (Lu

<sup>1</sup> Centro de Investigaciones Geofísicas (CIGEOF), Universidad Nacional de La Plata, Consejo Nacional de Investigaciones Científicas y Técnicas (CONICET), Argentina.

\* Contacto: [dperez@fcaglp.unlp.edu.ar](mailto:dperez@fcaglp.unlp.edu.ar)

et al., 2015). Due to the differences in two-way travel times observed between PP and PS data, it is necessary to match both datasets to the same time domain before performing any joint processes. This process, known as PP-PS registration, involves mapping (or "squeezing") the PS data to the PP time domain so that corresponding reflections in PP and PS images share the same two-way travel times (Gaiser, 1996; Fomel & Backus, 2003; Fomel et al., 2005; Compton & Hale, 2014; Geng et al., 2023). PP-PS registration is typically achieved by applying a warping function that minimizes the difference between the warped PS data and the PP data. This warping function can be directly derived from the  $v_P/v_S$  ratio, an important indicator of lithology and fluid properties (Stewart et al., 2003) often used to improve the characterization of unconventional reservoirs (Lines et al., 2005; Zuleta & Lawton, 2012).

Over the last few decades, numerous strategies have been developed for registering PP and PS data. Some methods are based on cross-correlation functions. For instance, Geis et al. (1990) use VSP and well log information to correlate seismic markers in time and depth, while Gaiser (1996) employ correlation to determine the long-wavelength components of the  $v_P/v_S$  ratio. Similarly, Fomel (2007) utilize a local attribute called local correlation to register multicomponent seismic data. Other approaches rely on global optimization algorithms to estimate warping functions. For example, Yuan et al. (2008) use simulated annealing to minimize the normalized cross-correlation between PP and PS data, and Liner and Clapp (2004) apply the Needleman-Wunsch algorithm (Needleman & Wunsch, 1970) for the same purpose. Fomel and Backus (2003) estimate a warping function by solving a least-squares objective function, while Zhang and Wang (2009) perturb an initial  $v_P/v_S$  solution to refine it. Similarly, Gao and Sacchi (2018) use a nonlinear optimization approach to estimate  $v_P/v_S$  ratios. Dynamic time warping (DTW) (Sakoe & Chiba, 1978) is another versatile method widely used in geophysical problems (Anderson & Gaby, 1983). Specifically, Hale (2013) and Compton and Hale (2014) use a modified DTW approach to successfully register PP and PS images and estimate  $v_P/v_S$  ratios.

Despite their effectiveness, these methods face unresolved challenges. Beyond differences in two-way travel time, PP and PS data exhibit disparities in signal-to-noise ratio (S/N), reflectivities, wavelet signatures (particularly in phase), and frequency bandwidth, with PS data often presenting a narrower and lower-frequency spectrum (Yuan et al., 2008). Additionally, as the  $v_P/v_S$  ratio varies with time and location, wavelet characteristics also change, further complicating the registration process. Direct warping of PS data often introduces non-stationarity. This non-stationarity arises from inevitable wavelet deformation, rendering the data unsuitable for subsequent processing (Chopra & Sharma, 2020; Geng et al., 2023). Many strategies aim to address these challenges by aligning PP and PS data while simultaneously correcting waveform deformations. For instance, Fomel and Backus (2003) use non-stationary spectral balancing, a deterministic wavelet correction scheme. Zhang and Wang (2009) propose an amplitude-preserving method to correct the frequency spectrum of the warped PS data. Similarly, Geng et al. (2023) combine dynamic time warping (DTW) with a zero-phase time-frequency adaptive shaping filter to achieve stationary solutions for the warped PS data.

The aforementioned correction strategies, while effective, can significantly increase computational complexity and may introduce artifacts, especially in noisy conditions. To address these challenges, we propose performing PP-PS registration in the reflectivity domain rather than the data domain. This approach inherently avoids waveform deformations, eliminating the need for post-processing corrections and thereby ensuring stationarity. By working in the reflectivity domain, we streamline the registration process and enhance the overall stability of PP-PS alignment.

The process begins by estimating wavelets for PP and PS data and computing sparse-spike reflectivities using the fast iterative shrinkage-thresholding algorithm (FISTA) (Beck & Teboulle, 2009). Registration is performed iteratively by adjusting the sparse-spike PS reflectivity until its corresponding seismic trace matches the PP trace. The velocity ratio is parameterized using monotonic cubic splines with a fixed number of knots at predefined times. The warping function is then obtained by integrating this velocity ratio. At each iteration, reflectivities are convolved with a stationary replacement wavelet to assess the match. The optimal knot coordinates are determined by solving the nonlinear, multimodal optimization problem with very fast simulated annealing (VFSA) (Ingber, 1989), minimizing a cost function that accounts for PP-PS differences while enforcing constraints to preserve prior information.

The final output consists of stationary PP and PS seismic datasets with aligned two-way travel times and consistent waveforms.

The paper is structured as follows. First, we present the theoretical background and outline the proposed method. Next, we test its performance on a 1D synthetic example derived from well log data, performing a parameter-sensitivity analysis, and comparing the results with DTW. We then validate the method on more complex synthetic 2D data derived from actual field PP data. Finally, we discuss our findings and summarize the key conclusions.

## THEORY AND METHODS

### PP-PS registration in the data domain

The registration of PP and PS data involves mapping the PS data to the PP time domain so that corresponding reflections in both images exhibit similar two-way travel times (Geng et al., 2023). This mapping can be carried out by finding an appropriate warping function,  $\tau(t)$ , that relates the PP and PS time domains, such that

$$s_{PP}(t) - s_{PS}(\tau(t)) \approx 0, \quad (1)$$

where  $s_{PP}(t)$  and  $s_{PS}(t)$  denote the PP and PS seismic traces, respectively.

Assuming zero-offset data, the two-way travel times for PP and PS waves along an infinitesimal depth interval  $dz$  are given by  $dt = 2dz/v_P$  and  $d\tau = dz/v_P + dz/v_S$ . From these, we obtain  $d\tau/dt = (1 + \gamma(t))/2$ , where  $\gamma(t)$  is the  $v_P/v_S$  ratio in the PP time domain. This ratio is generally time-dependent, reflecting changes in velocities with depth caused by lithological variations. Integrating from an initial time  $t_0$  this equation yields

$$\tau(t) = \int_{t_0}^t \frac{1 + \gamma(t')}{2} dt', \quad (2)$$

As noted earlier, many studies have addressed PP-PS registration by estimating  $\tau(t)$  or  $\gamma(t)$ , but working in the data domain often requires additional corrections for waveform deformations (Fomel & Backus, 2003; Zhang & Wang, 2009; Geng et al., 2023). These corrections increase computational complexity and may introduce artifacts. Registering in the reflectivity domain eliminates these issues, as reflectivities remain unaffected by waveform distortions, thereby ensuring stationarity.

### PP-PS registration in the reflectivity domain

The proposed strategy involves two stages: first, sparse-spike reflectivities  $\mathbf{r}_{PP}$  and  $\mathbf{r}_{PS}$  are estimated from the seismic traces  $\mathbf{s}_{PP}$  and  $\mathbf{s}_{PS}$ ; second, the warping function  $\tau(t)$  is derived to transform  $\mathbf{r}_{PS}$  into  $\hat{\mathbf{r}}_{PS}$ , ensuring the envelope of the warped trace  $\hat{\mathbf{e}}_{PS}$  matches that of the corresponding PP trace. Envelopes are used instead of the data itself to avoid sensitivity to polarity mismatches between PP and PS data (Gao & Sacchi, 2018).

#### *First stage: Sparse-spike deconvolution*

Assuming the validity of the convolutional model (Yilmaz, 2001, e.g.), a noisy seismic trace  $\mathbf{s}$  can be expressed as

$$\mathbf{s} = \mathbf{W}\mathbf{r} + \mathbf{n}, \quad (3)$$

where  $\mathbf{r}$  is the reflectivity,  $\mathbf{W}$  is the convolution matrix associated with the stationary source wavelet  $\mathbf{w}$ , and  $\mathbf{n}$  is the additive noise. We further assume that, given an estimate of the seismic wavelet, a sparse-spike reflectivity model exists that honors the observed data. Sparse solutions lead to sharply resolved reflectors that overcome the band-limitation of classical  $l_2$ -norm solutions (Debye & van Riel, 1990). Although the real subsurface structure is continuous (Cooke & Schneider, 1983), derived reflectivities from well-logs show that, in general, the main lithological units can be associated with

sparsely distributed large reflection coefficients (Walden & Hosken, 1986), leading to deconvolution approaches that rely on the non-Gaussianity assumption (Wiggins, 1978; Oldenburg et al., 1983; Robinson & Ebro, 1996; Sacchi et al., 1996). In this framework, the wavelet is assumed stationary and reasonably well estimated. While moderate inaccuracies in its estimation can be tolerated, large systematic errors (e.g., bandwidth or phase bias) may compromise the stability of the inversion and the reliability of the recovered reflectivity.

Numerous algorithms exist to estimate sparse-spike solutions for  $\mathbf{r}$  (Taylor et al., 1979; Oldenburg et al., 1983; Sacchi, 1997; Pérez & Velis, 2011; Pérez et al., 2013; Pérez et al., 2017; Pérez & Velis, 2018; Kazemi, 2018; Sui & Ma, 2020; Pereg et al., 2020; Chai et al., 2021). In particular, we use the method described by Pérez et al. (2013), where a stable and sparse-spike solution for  $\mathbf{r}$  is obtained by solving

$$\hat{\mathbf{r}} = \arg \min_{\mathbf{r}} \left\{ \|\mathbf{W}\mathbf{r} - \mathbf{s}\|_2^2 + \lambda \|\mathbf{r}\|_1 \right\}. \quad (4)$$

Here,  $\|\mathbf{W}\mathbf{r} - \mathbf{s}\|_2^2$  measures the differences between the observed and modeled data (misfit), while the trade-off parameter  $\lambda$  controls the sparsity of the reflectivity and must be selected in advance. To determine its value, we construct the L-curve (also known as the Pareto curve) (van den Berg & Friedlander, 2008; Hennenfent et al., 2008) by performing the inversion for a range of trial  $\lambda$  values and plotting the resulting  $l_1$ -norm against the misfit. The optimal  $\lambda$  is then chosen at the point on the curve that best balances the misfit and the  $l_1$ -norm, ensuring an accurate fit to the data while preserving geological realism.

For PP-PS registration, equation 4 must be solved twice to obtain sparse reflectivities for both PP and PS traces. We use FISTA (Beck & Teboulle, 2009), an extension of the classical gradient algorithm for solving large-scale linear inverse problems. FISTA relies only on matrix-vector multiplications at each iteration, avoiding matrix inversions, which makes it both simple and computationally efficient. For further details, see Pérez et al. (2013).

### Second stage: Warping function estimation

After the first stage, we obtain the sparse-spike reflectivities  $\mathbf{r}_{PP}$  and  $\mathbf{r}_{PS}$  from the seismic traces  $\mathbf{s}_{PP}$  and  $\mathbf{s}_{PS}$ , and their respective wavelets  $\mathbf{w}_{PP}$  and  $\mathbf{w}_{PS}$ . Using a replacement wavelet  $\hat{\mathbf{w}}$ , we create a stationary PP seismic trace  $\hat{\mathbf{s}}_{PP}$ . While  $\mathbf{w}_{PP}$  can be used as the replacement wavelet, experimenting with alternatives, such as Ormsby wavelets, is recommended. In our experience, replacement wavelets with flat spectra and modest side lobes generally produce satisfactory results.

The reflectivity  $\mathbf{r}_{PS}$  is mapped to the PP time domain using the warping function  $\tau(t)$ , derived from  $\gamma(t)$  as defined in equation 2. We represent  $\gamma(t)$  using monotonic cubic splines interpolation (Fritsch & Butland, 1984) with  $K$  values (or knots)  $\mathbf{g} = [g_1, g_2, \dots, g_K]$ . For simplicity, the times  $t_1 < t_2 < \dots < t_K$  corresponding to the knots are fixed and equally spaced within the data time window. Within each interval  $[t_k, t_{k+1}]$ ,  $\gamma(t)$  is expressed as a cubic polynomial, with its coefficients determined by ensuring continuity of  $\gamma(t)$  and its first and second derivatives at the times  $t_k$ , as well as satisfying the monotonicity constraint.

The warping function  $\tau(t)$  is applied to each time sample of  $\mathbf{r}_{PS}$ , producing the perturbed PS reflectivity  $\hat{\mathbf{r}}_{PS}$ , given by  $\hat{r}_{PS}(t) = r_{PS}(\tau(t))$ . Finally, the perturbed reflectivity  $\hat{\mathbf{r}}_{PS}$  is convolved with the replacement wavelet  $\hat{\mathbf{w}}$  to generate the stationary warped PS trace  $\hat{\mathbf{s}}_{PS}$ . The knot values  $\mathbf{g}$  are estimated by solving the following optimization problem:

$$\hat{\mathbf{g}} = \arg \min_{\mathbf{g}} \left\{ (1 - \mu) [1 - \rho(\hat{\mathbf{e}}_{PP}, \hat{\mathbf{e}}_{PS})] + \mu E(\hat{\gamma}, \gamma_0) \right\}, \quad (5)$$

where  $\rho(\hat{\mathbf{e}}_{PP}, \hat{\mathbf{e}}_{PS})$  is the normalized correlation between the envelopes  $\hat{\mathbf{e}}_{PP}$  and  $\hat{\mathbf{e}}_{PS}$  of the seismic traces  $\hat{\mathbf{s}}_{PP}$  and  $\hat{\mathbf{s}}_{PS}$ ,  $E(\hat{\gamma}, \gamma_0)$  is the normalized mean squared error between  $\hat{\gamma}$  and a pre-selected reference trend  $\gamma_0$ , and  $\mu$  ( $0 \leq \mu \leq 1$ ) is a trade-off parameter that weights the two terms and must be chosen beforehand. If  $\mu$  is too large the estimated  $\hat{\gamma}$  will overfit the  $\gamma_0$  in detriment of a correct registration of the envelopes of the traces. On the other hand, a value of  $\mu$  too small may result in

solutions of  $\hat{\gamma}$  that correctly register the envelopes, but without physical meaning.

The first term in [equation 5](#) quantifies the misfit between the PP and PS data. Unlike conventional methods that rely on the  $L_2$ -norm, we use normalized correlation, which is insensitive to scale differences and thus better suited to this problem. Envelopes are computed as

$$\mathbf{e} = \sqrt{\mathbf{s}^2 + H(\mathbf{s})^2}, \quad (6)$$

where  $H(\cdot)$  is the Hilbert transform (Taner et al., 1979). The second term in [equation 5](#) acts as a regularization term, ensuring that the proposed  $v_P/v_S$  ratio retains physical meaning by enforcing that  $\hat{\gamma}$ , the estimated  $\gamma(t)$  evaluated at PP data time samples, remains close to  $\gamma_0$ . The trade-off parameter  $\mu$  must be set in advance. Since both terms in the cost function and  $\mu$  are within  $[0, 1]$ , its selection is straightforward and independent of the time window size, number of knots, or other parameters. For  $\mu = 0$ , only waveform alignment is considered; for  $\mu = 1$ , the solution strictly adheres to  $\gamma_0$ . Intermediate values (e.g.,  $\mu = 0.2$ ) balance both terms. The [equation 5](#) defines a nonlinear, multimodal optimization problem, which is efficiently solved using very fast simulated annealing (VFSA) (Ingber, 1989).

### *The algorithm step-by-step*

1. Estimate the sparse-spike reflectivities  $\mathbf{r}_{PP}$  and  $\mathbf{r}_{PS}$  from the seismic traces  $\mathbf{s}_{PP}$  and  $\mathbf{s}_{PS}$ , and their respective wavelets  $\mathbf{w}_{PP}$  and  $\mathbf{w}_{PS}$ .
2. Using a replacement wavelet  $\hat{\mathbf{w}}$ , generate the stationary PP seismic trace  $\hat{\mathbf{s}}_{PP}$  and compute its envelope  $\hat{\mathbf{e}}_{PP}$ .
3. Define the reference trend  $\gamma_0$ , the trade-off parameter  $\mu$ , and the number of knots  $K$ .
4. For each VFSA iteration:
  - a) Propose a new  $\gamma(t)$  and derive the corresponding warping function  $\tau(t)$ .
  - b) Perturb the reflectivity  $\mathbf{r}_{PS}$  using  $\tau(t)$  to obtain the perturbed reflectivity  $\hat{\mathbf{r}}_{PS}$ .
  - c) Convolve  $\hat{\mathbf{r}}_{PS}$  with the replacement wavelet  $\hat{\mathbf{w}}$  to generate the stationary PS trace  $\hat{\mathbf{s}}_{PS}$  and compute its envelope  $\hat{\mathbf{e}}_{PS}$ .
  - d) Evaluate the cost function ([equation 5](#)).
  - e) Check for convergence or stopping criteria (e.g., maximum number of iterations).

Regarding computational cost, processing each trace takes a few seconds on a standard PC, making it feasible for most applications. The prototype was implemented in Python for flexibility, as computational efficiency was secondary to method validation. It can be optimized in higher-performance languages like C, Fortran, or Julia for greater efficiency. Additionally, we use around 10000 VFSA iterations per case for simplicity, though convergence is usually achieved much earlier.

## NUMERICAL RESULTS

We evaluate the proposed method using two examples. First, we test it on 1D seismic data derived from well logs, analyzing its performance under different parameter settings and comparing it to DTW. Next, we apply it to a 2D dataset, where the PP section comes from field data, and the PS section is synthetically generated. This allows us to assess its performance in a more complex scenario, focusing on lateral continuity and geological consistency.

### 1D example

#### *Data generation*

The data was created from actual well log information ([Figure 1a](#) to [Figure 1d](#)). Gray lines represent observed data, and black lines show the Backus average (Backus, 1962), a necessary step to upscale

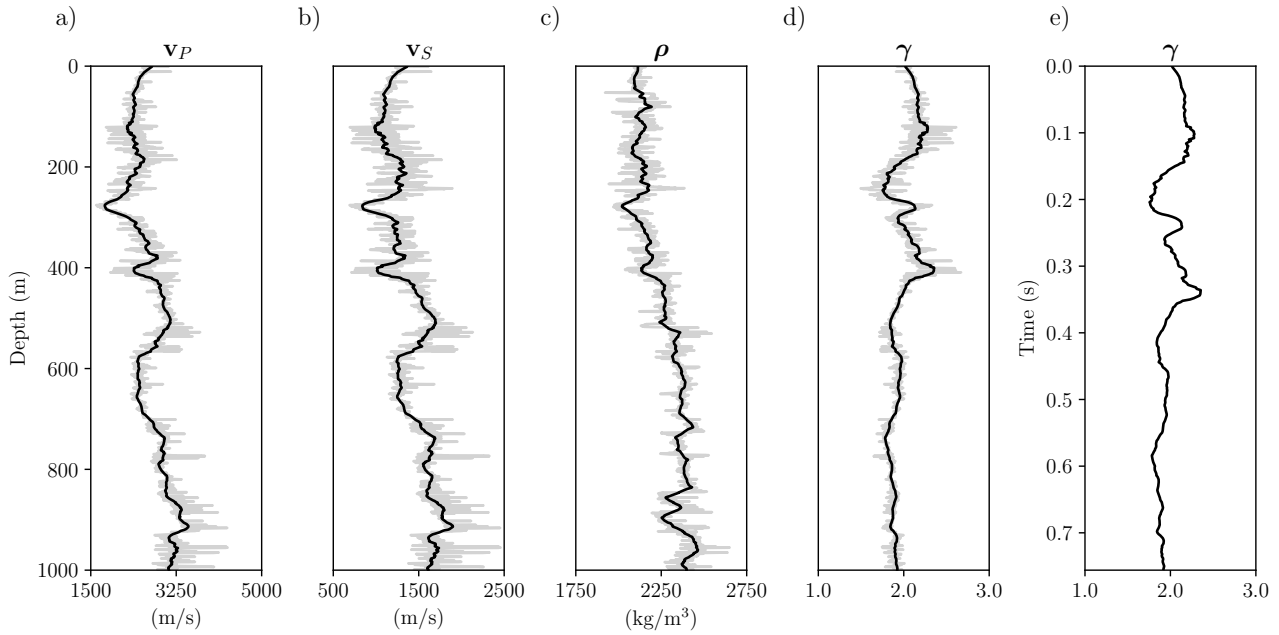


**Figure 1.** Well log information: a) P-wave velocity, b) S-wave velocity, c) density, d)  $v_P/v_S$  ratio, and e)  $v_P/v_S$  ratio in the PP time domain. Gray lines represent observed data, and black lines show the Backus average.

the logs to seismic wavelengths (Lindsay & Van Koughnet, 2001). Figure 1e also shows  $\gamma$  in the PP time domain, which will later serve as a reference to evaluate the quality of the registration.

Using the upscaled P-wave and S-wave velocities and density, we generated PP and PS reflectivities based on the exact Zoeppritz equations (Zoeppritz, 1919), considering incidence angles ranging from  $0^\circ$  to  $40^\circ$ . Depth-to-time conversion was performed using a depth sampling interval of  $\Delta z = 0.1$  m, with a time sampling of 2 ms. The synthetic PP and PS seismic traces were then obtained by convolving the angle-dependent reflectivities with Ricker wavelets (Ricker, 1940), using central frequencies of 30 Hz for PP and 20 Hz for PS, the latter being phase-rotated by  $45^\circ$ . To simulate realistic conditions, we added band-limited Gaussian noise, setting the signal-to-noise ratio (S/N) to 5 for PP data and 1 for PS data. The resulting angle gathers are displayed in Figure 2, along with the corresponding stacked traces,  $\mathbf{s}_{PP}$  and  $\mathbf{s}_{PS}$ , which were used for registration.

### Registration results

Given the seismic data, the first step in the proposed registration process is estimating sparse-spike reflectivities. Figure 3a to Figure 3d show the corresponding sparse-spike reflectivities after solving equation 4 with  $\lambda = 0.01$ , and the reconstructed traces. They closely match the observed data, confirming that the estimated reflectivities honor the input data and are suitable for registration. Figure 3e shows the estimated wavelets  $\mathbf{w}_{PP}$  and  $\mathbf{w}_{PS}$ , along with the replacement  $\hat{\mathbf{w}}$ , an Ormsby wavelet with a frequency bandwidth of 5-15-55-75 Hz. To estimate  $\mathbf{w}_{PP}$  and  $\mathbf{w}_{PS}$ , in this work we obtain zero phase wavelets by calculating the amplitude spectrum of the trace and performing the inverse Fourier transform. We also apply a Hamming taper to smooth the average spectrum and to improve the estimation. The phase shifts were estimated by the method proposed by Gelpi et al. (2019).

Given the stochastic nature of VFSA, in each case we performed 100 realizations of the registration, using different random seeds to assess the robustness and reproducibility of the solutions. For this example we used  $K = 12$ ,  $\mu = 0.2$ , a constant reference trend  $\gamma_0 = 2.0$ , and constrained the knot values  $g_k$  to the range  $[1.0, 3.0]$ . Figure 4 shows the corresponding PP-PS registration results. The 100 warped reflectivities show very little dispersion (Figure 4b), align well with the actual  $\mathbf{r}_{PS}$  (Figure 3b), and preserve the reflectors' amplitudes, ensuring the preservation of the warped traces amplitudes. The results confirm that the proposed method accurately aligns the PS data: the warped traces  $\hat{\mathbf{s}}_{PS}$

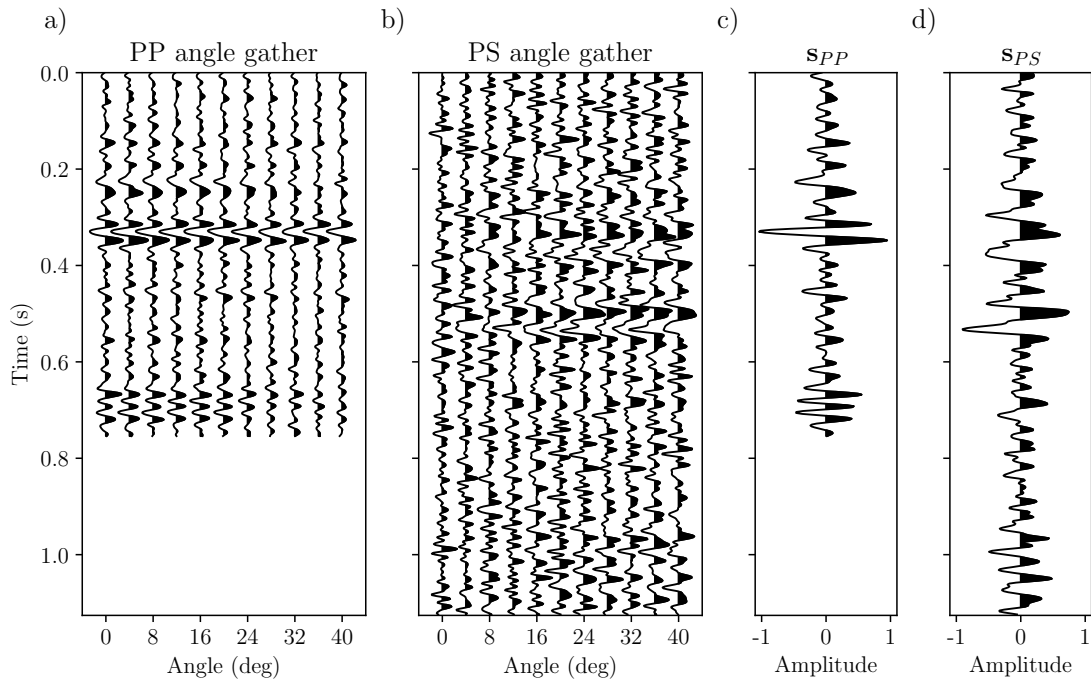


**Figure 2.** Synthetic data generated from well log information: a) PP angle gather, b) PS angle gather, c) PP stack, and d) PS stack.

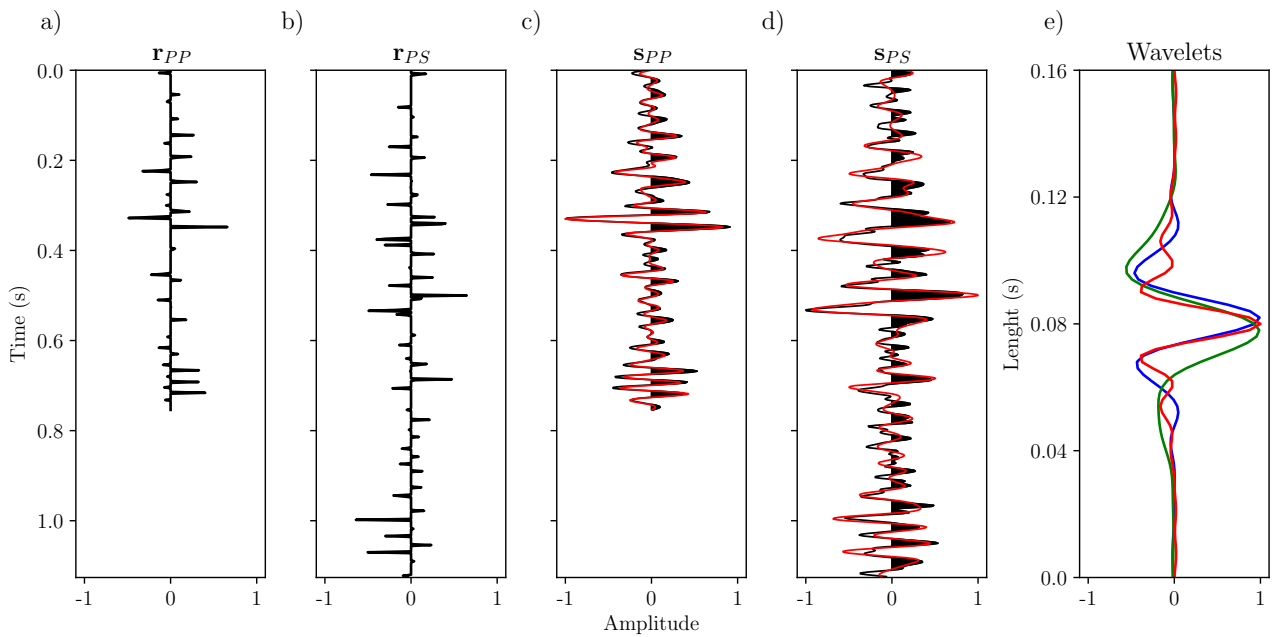


**Figure 3.** a) and b) Estimated reflectivities for PP and PS stacks. c) and d) Observed data (black) and reconstructed data (red). e) Estimated (blue and green) and replacement (red) wavelets.

and their envelopes are consistent across realizations and closely resemble the corresponding  $\hat{\mathbf{s}}_{PP}$  data, aside from scale differences.

### Comparison with DTW

For comparison, Figure 4e shows the registration obtained using DTW (Sakoe & Chiba, 1978), as described by Herrera et al. (2014). This strategy applies corrections directly to  $\mathbf{s}_{PS}$  to align it with  $\mathbf{s}_{PP}$  and employs the Sakoe-Chiba band global constraint to prevent unrealistic solutions, given as result

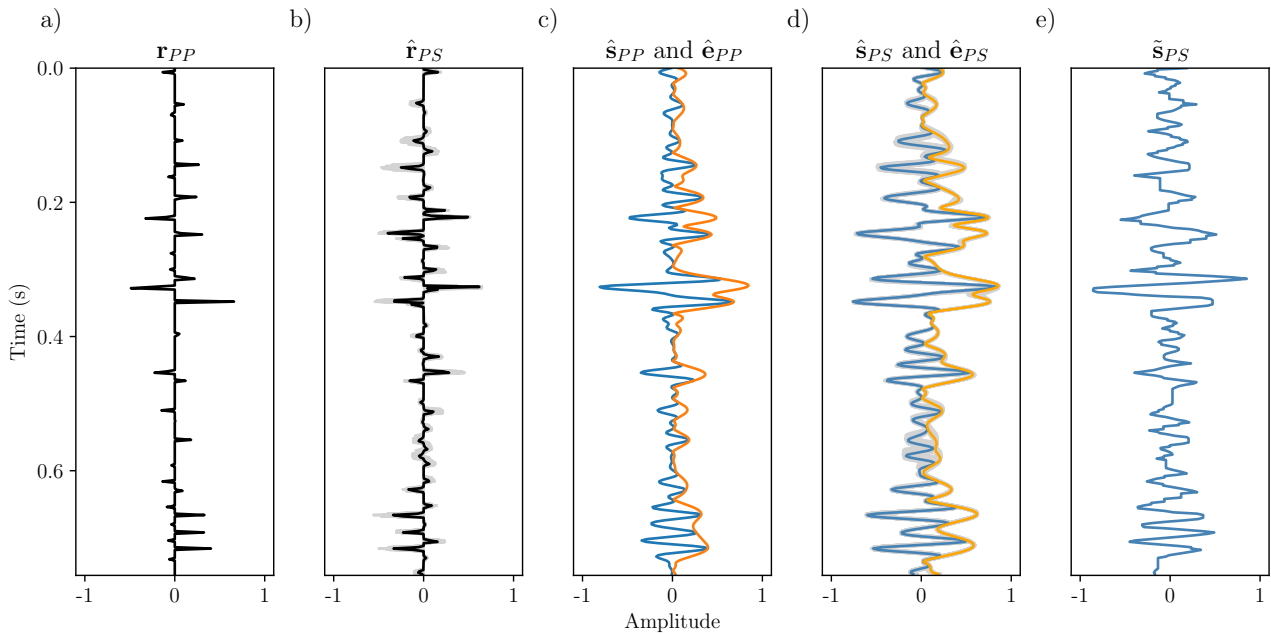


**Figure 4.** PP-PS registration for  $K=12$ . a) PP reflectivity. b) Registered PS reflectivities: 100 individual solutions in gray and their mean value in black. c) Reconstructed PP data and its envelope. d) Registered PS data: 100 individual solutions in gray, mean value in blue, and envelopes in orange. e) PP-PS registration using DTW.

the registered  $\tilde{\mathbf{s}}_{PS}$  trace. As observed, this approach introduces artifacts and waveform distortions that can mislead geological interpretations.

Figure 5e compares the mean solutions obtained with the proposed algorithm and DTW for the 0.1–0.4 s interval. A clear mismatch emerges between the DTW-warped trace  $\tilde{\mathbf{s}}_{PS}$  and the reflectivity  $\hat{\mathbf{r}}_{PS}$ —a discrepancy absent in our method’s warped trace ( $\hat{\mathbf{s}}_{PS}$ ). Since DTW operates directly on seismic traces, it compels  $\tilde{\mathbf{s}}_{PS}$  to adopt the polarity of  $\mathbf{s}_{PP}$ , disregarding the true polarity of the PS reflectors. Moreover, misalignments can occur even beyond polarity reversals: in cases of large amplitude contrasts, DTW may align a PS reflector with the wrong PP counterpart based on amplitude similarity rather than true geological correspondence. This limitation is not unique to DTW but is inherent to any method that warps  $\mathbf{s}_{PS}$  to match  $\mathbf{s}_{PP}$  directly, rather than using envelopes as proposed here.

In this case,  $\hat{\mathbf{r}}_{PS}$  was obtained directly from the  $v_P/v_S$  ratio derived from the well log, rather than from the estimated  $\gamma(t)$  solutions. Since this reflectivity was not derived through registration, we consider it the actual  $\mathbf{r}_{PS}$  reflectivity in the PP time domain—a faithful representation of the subsurface geology.

Finally, Figure 6 compares the amplitude spectra of the estimated wavelets, the PP and PS data, and their registered versions. The proposed method preserves spectral consistency while minimizing high-frequency artifacts, whereas the DTW approach introduces unwanted spectral content due to waveform distortions. In particular, by convolving both PP and PS reflectivity estimates with the same replacement wavelet, the proposed approach ensures that the registered data share the same frequency content, effectively compensating for the lower resolution of the PS data.

#### Parameter selection: Sensitivity analysis

For the registration process, we first select the number of knots  $K$ , the reference trend  $\gamma_0$ , and the trade-off parameter  $\mu$ . Increasing  $K$  may increase the normalized correlation but can lead to reflectivities with no physical meaning, while choosing  $K$  too small may result in solutions that do not align well. This trade-off is similar to challenges in automatic well-tying problems (Herrera et al., 2014; Gelpi et al., 2020). Regarding the trade-off parameter  $\mu$ , conservative values are recommended. If  $\mu$  is too large, the estimated  $\hat{\gamma}$  will closely follow  $\gamma_0$ , which, depending on its quality, may reduce registration

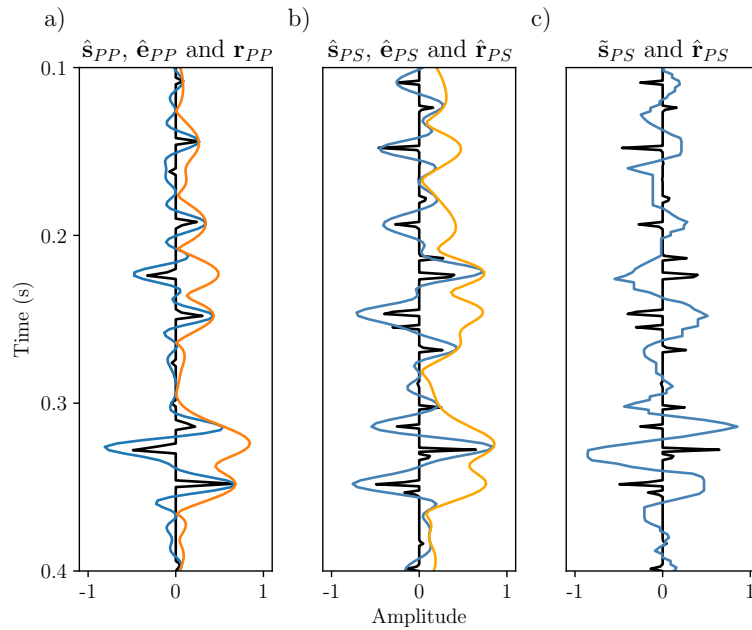


**Figure 5.** a) PP stacked trace, envelope, and sparse-spike reflectivity. b) Mean PS warped trace, envelope, and sparse-spike reflectivity in the PP time domain. c) PS warped trace from DTW and corresponding sparse-spike reflectivity in the PP time domain.

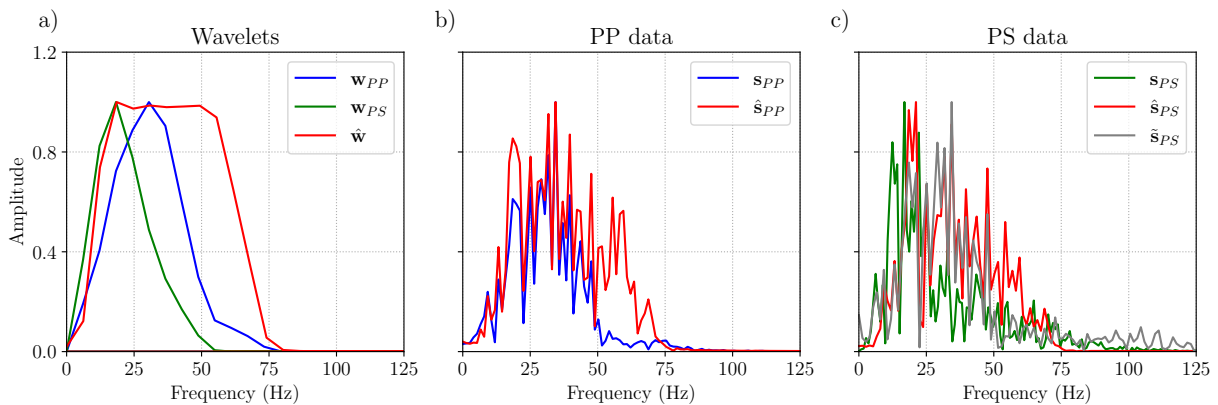


**Figure 6.** Amplitude spectra of: a) estimated wavelets and the replacement wavelet; b) PP data before and after registration; c) PS data before and after registration.

accuracy.

To analyze the actual impact of  $K$  and  $\mu$  on the estimated solutions, we performed registrations with  $K = 8, 12,$  and  $16$ , testing various  $\mu$  values for each. The results are summarized in [Table 1](#). As observed, both the number of knots ( $K$ ) and the regularization parameter ( $\mu$ ) influence the estimated solutions, though differences across cases are minor. Increasing  $\mu$  strengthens the regularization term, enforcing consistency with  $\gamma_0$  and improving the normalized gamma correlation  $\rho(\hat{\gamma}, \gamma)$ , which measures the similarity between the estimated  $\hat{\gamma}$  and the actual  $\gamma$  depicted in [Figure 1e](#). Envelope correlation values  $\rho(\hat{\mathbf{e}}_{PP}, \hat{\mathbf{e}}_{PS})$  remain high across all cases, confirming robust alignment regardless of parameter selection. This stability simplifies parameter selection, as moderate variations in  $K$  and  $\mu$  have little impact. Notably, using  $\gamma_0$  alone yields a correlation of  $0.753$ , indicating that most alignment comes from the trend itself. While excessive regularization slightly reduces  $\rho(\hat{\mathbf{e}}_{PP}, \hat{\mathbf{e}}_{PS})$ , larger  $K$  improves it but may decrease  $\rho(\hat{\gamma}, \gamma)$  significantly, specially for small  $\mu$ , likely due to overfitting. Standard deviations remain low for  $\rho(\hat{\mathbf{e}}_{PP}, \hat{\mathbf{e}}_{PS})$ , while greater variability is observed in  $\rho(\hat{\gamma}, \gamma)$  at low  $\mu$ . A good balance between accuracy and stability occurs at  $K = 12$  and  $\mu = 0.2$ , which yield high  $\rho(\hat{\gamma}, \gamma)$  while maintaining strong envelope correlation.

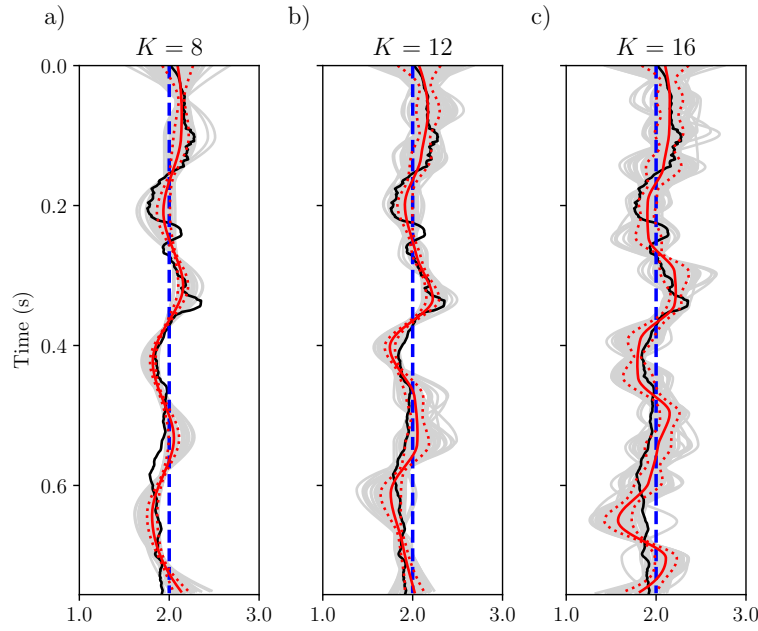


**Figure 7.** Estimated  $\hat{\gamma}$  using  $\mu = 0.2$  for a)  $K = 8$ , b)  $K = 12$ , and c)  $K = 16$ . Gray lines represent the individual solutions obtained by VFSA, the red line shows their mean value and the dotted line the standard deviation. The actual  $\gamma$  is shown in black, and the reference trend  $\gamma_0$  is shown as a dashed blue line.

Figure 7 shows the estimated  $v_P/v_S$  ratios from 100 realizations for the three tested  $K$  values with  $\mu = 0.2$ , along with the mean solutions and the actual  $\gamma$  (Figure 1e). The results indicate that all configurations produced high correlations and relatively low variability (except for  $K = 16$ ), demonstrating the robustness of the approach. In all cases, the mean solutions provide reasonable approximations of  $\gamma$ , accurately capturing the general trend across most time intervals. Below 0.5 s, where weaker reflectors and lower S/N dominate, slight discrepancies emerge, but the solutions remain stable overall. Increasing  $K$  or adjusting  $\mu$  further does not significantly improve the estimated  $\gamma$ , as the data lacks sufficient information to constrain the velocity ratio beyond current estimates. A more informative prior  $\gamma_0$  would be required to refine the solution further.

Figure 8 shows  $d(t) = \tau(t) - l(t)$ , where  $\tau(t)$  is estimated using equation 2 and  $l(t)$  is the linear trend that unites the first and last sample of the PP and PS data, that is

$$l(t) = \tau_0 + \left( \frac{\tau_f - \tau_0}{t_f - t_0} \right) (t - t_0), \quad (7)$$

where  $t_f$  and  $\tau_f$  are the last time samples of PP and PS data respectively. We choose to show  $d(t)$  because the almost rectilinear behavior of the estimated  $\tau(t)$  functions, which makes difficult to directly observe differences between individual solutions. The grey curves show  $d(t)$  for all knots and

**Table 1.** Mean and standard deviation after 100 realizations (transposed). The best balance between accuracy and stability occurs at  $K = 12$  and  $\mu = 0.2$ . For reference,  $\rho(\hat{\mathbf{e}}_{PP}, \hat{\mathbf{e}}_{PS}) = 0.753$  for  $\gamma = \gamma_0$  in all cases.

$\mu$	$K = 8$				$K = 12$				$K = 16$			
	$\rho(\hat{\mathbf{e}}_{PP}, \hat{\mathbf{e}}_{PS})$		$\rho(\hat{\gamma}, \gamma)$		$\rho(\hat{\mathbf{e}}_{PP}, \hat{\mathbf{e}}_{PS})$		$\rho(\hat{\gamma}, \gamma)$		$\rho(\hat{\mathbf{e}}_{PP}, \hat{\mathbf{e}}_{PS})$		$\rho(\hat{\gamma}, \gamma)$	
	Mean	Std.	Mean	Std.	Mean	Std.	Mean	Std.	Mean	Std.	Mean	Std.
0.1	0.883	0.003	0.623	0.116	0.886	0.003	0.648	0.114	0.890	0.003	0.484	0.102
0.2	0.881	0.003	0.713	0.078	<b>0.883</b>	<b>0.002</b>	<b>0.731</b>	<b>0.102</b>	0.887	0.004	0.559	0.098
0.3	0.877	0.003	0.726	0.071	0.879	0.002	0.771	0.061	0.882	0.003	0.642	0.092
0.4	0.875	0.003	0.722	0.072	0.876	0.002	0.759	0.060	0.877	0.003	0.652	0.091

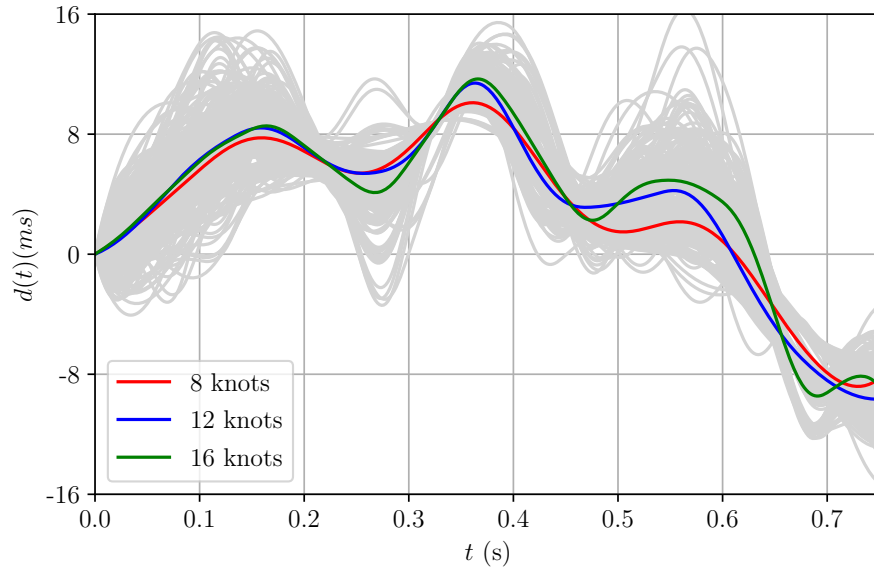


**Figure 8.** Time shifts of the estimated  $\tau(t)$  relative to the linear trend: gray lines represent the 100 individual solutions, and the colored lines show the mean values for each  $K$ .

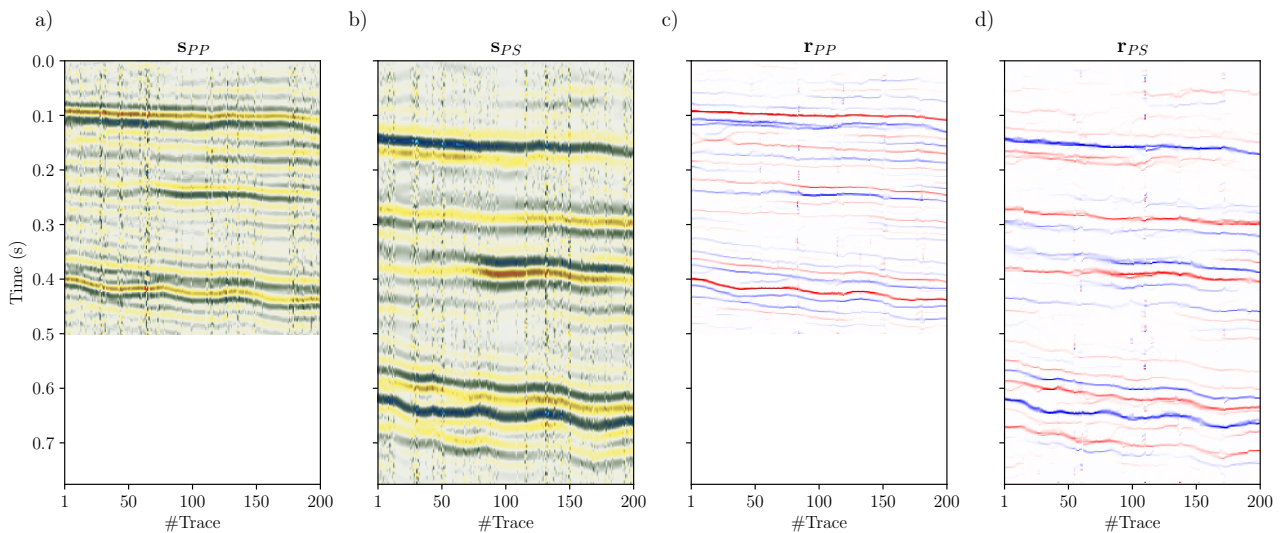


**Figure 9.** a) Field PP stack section. b) Synthetic PS stack section. c) Sparse-spike reflectivity from PP data. d) Sparse-spike reflectivity from synthetic PS data.

realizations. As can be seen, despite the differences in the estimated  $\gamma(t)$  (Figure 7), the derived  $\tau(t)$  functions show similar behavior and low dispersion between each other, and only deviate from  $l(t)$  by a few milliseconds.

## 2D example

### Data generation

Figure 9a shows a noisy field PP stack section with 200 traces over a 0.5 s time window and a 2 ms sampling interval. This section was obtained from a noiseless PP stack section, to which two types of noise were added to test the proposed method against challenging conditions: i) gaussian noise with SNR=10 to the whole section and ii) gaussian noise with SNR between 3 and 5 to random traces. From this, we estimated the sparse-spike reflectivity section in Figure 9c using FISTA, applying total variation regularization (Rudin et al., 1992; Chambolle, 2004; Beck & Teboulle, 2009) to enhance

lateral continuity (Pérez & Velis, 2018) instead of  $l_1$ -regularization as in the 1D example. As we use the same  $\lambda$  trade-off parameter for the whole section, part of the noise filtered to the estimated sparse-spike reflectivity.

Since no field PS data was available, we generated synthetic PS data from the estimated PP reflectivity. We derived the velocity, density, and  $\gamma$  blocky models shown in Figure 10, where P-wave velocity came from the PP reflectivity estimated from the noiseless PP section, S-wave velocity was obtained using Castagna's relationship (Castagna et al., 1985), and density from Gardner's equation (Gardner et al., 1974). Model amplitudes were calibrated to ensure the PP synthetic stack section matched the field PP section in Figure 9a.

Using this model, we generated 200 PS angle gathers with incidence angles from  $0^\circ$  to  $40^\circ$ , computing reflectivities with the full Zoeppritz equations (Zoeppritz, 1919). PS seismic traces were obtained by convolving these reflectivities with a Ricker wavelet at 20 Hz central frequency.

The resulting synthetic PS stack section, which was contaminated with the same type of noise as the PP stack section, is shown in Figure 9b, with the corresponding sparse-spike reflectivity section in Figure 9d, estimated using FISTA and total variation.

### Registration results

The registration was performed using the estimated sparse-spike reflectivity sections and an Ormsby wavelet with a frequency bandwidth of 5-15-55-75 Hz as the replacement wavelet. For this example, we used  $K = 12$ ,  $\mu = 0.2$ , and a constant reference trend of  $\gamma_0 = 2.0$  across the entire section, with knots  $g_k$  constrained to the range  $[1.0, 3.0]$ . Given the smooth lateral variations in the data, we optimized the registration process for efficiency. Instead of registering each trace individually, we performed registration every 50 traces. The estimated knot coordinates were then interpolated using splines to obtain the  $\hat{\gamma}$  ratios for the remaining traces. This approach not only improved computational efficiency but also enhanced the lateral continuity of the solutions.

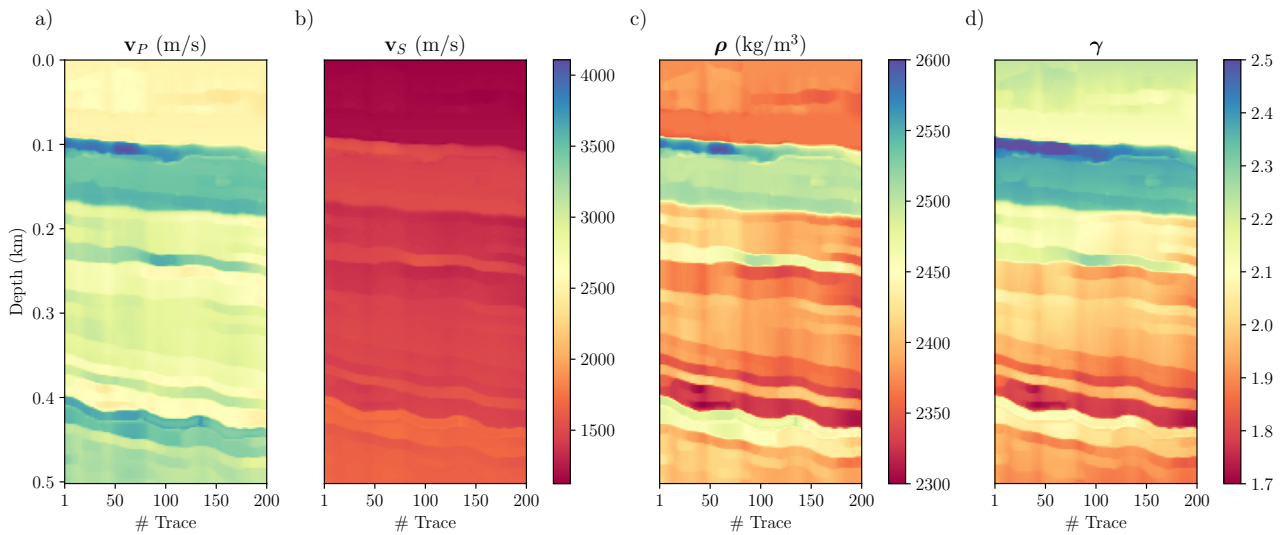
Figure 11a and Figure 11b show the stationary PP section and the registered PS section. The results confirm that the proposed method successfully aligned the PS data, with the registered PS section closely matching the PP section. Reflectors exhibit good lateral continuity, with no artifacts or wavelet distortions. Due to the sparse-spike deconvolution step, the registered sections show less noise than the observed ones. The correlation between the envelopes of the PP and registered PS sections was 0.837, significantly higher than the 0.598 obtained when using the initial reference trend alone. This highlights the importance of proper registration in achieving accurate alignment.

Figure 11c shows the estimated  $\hat{\gamma}$  ratio section, which maintains lateral continuity and appropriate amplitudes. Its overall trend closely follows the actual  $\gamma$  ratio model shown in Figure 10d. Finally, Figure 11d compares the amplitude spectra of the PP and PS data before and after registration. The proposed method preserves spectral consistency while improving the bandwidth of the registered PS data.

## DISCUSSION

The proposed method provides several practical advantages over conventional registration approaches such as DTW. The estimation of reflectivity through *sparse-spike* deconvolution not only enables the registration of PS data but also reduces noise, improving the overall quality of the signal. The physically constrained parameterization of the  $\gamma(t)$  function favors solutions that are geologically plausible, while the use of a replacement wavelet allows for frequency enhancement without introducing inconsistencies between the registered PP and PS sections. Combined, these features help preserve waveform integrity and ensure greater consistency for subsequent processing and interpretation.

The sensitivity analysis demonstrates that the selection of  $K$  and  $\mu$  is not critical, as moderate variations in these parameters yield consistently high envelope correlations and stable  $\hat{\gamma}(t)$  estimates. In this



**Figure 10.** Blocky models used to generate synthetic PS data. a) P-wave velocity. b) S-wave velocity. c) Density. d) Actual  $\gamma$  ratio field.

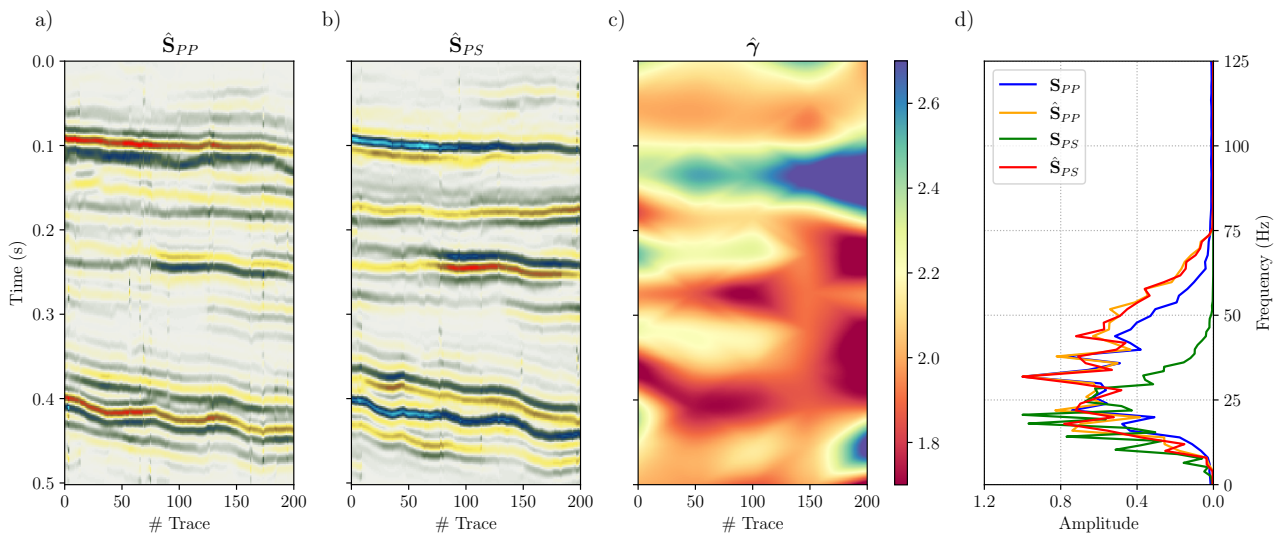


**Figure 11.** PP-PS registration results. a) Stationary PP section. b) Registered PS section. c) Estimated  $\hat{\gamma}$  ratio section. d) Amplitude spectra before and after registration.

context, our goal is not to force a very high correlation but to achieve a reasonable PP–PS alignment that preserves waveform integrity and spectral consistency, enabling reliable subsequent analysis and interpretation. This is analogous to the well-tying process, where a perfect match between observed and synthetic traces is neither expected nor necessarily desirable, since they are inherently different. Consequently, we consider that further analysis to determine optimal  $K$  and  $\mu$  values is unnecessary. The values proposed here can be used as practical guidelines for other applications, with the understanding that alternative choices will produce similar results regardless of geological complexity.

Regarding the sensitivity of the proposed method to wavelet-estimation errors, while this is a common concern in deconvolution-based workflows, our synthetic experiments show that moderate phase or amplitude errors in the estimated wavelets have limited impact on the estimated  $\gamma(t)$  and the alignment quality. This is mainly because the registration is performed on envelopes, making it less sensitive to small phase mismatches. In the presented numerical examples the same replacement wavelet was applied to both PP and PS reflectivities. This was a personal choice, as one may use any of the estimated wavelet from the PP or PS data for the registration process. In any case, the selection of the

wavelet is not critical as far as it does not depart too much from the actual wavelet present in the data. Large, systematic errors in the wavelet (e.g., incorrect bandwidth, strong phase bias) could affect the reflectivity estimation and, consequently, the registration. In such cases, additional care in wavelet estimation—possibly involving external information such as well ties—would be advisable.

The second numerical example relied on synthetic PS data generated from field PP data. Although not ideal, this synthetic dataset reasonably approximates real-world conditions, allowing an effective assessment of the method. While it lacks the full complexity of field PS data, it retains key geological and seismic characteristics, making it suitable for evaluation. We expect similar results on real field data, as the method accounts for realistic noise levels and parameter variations. However, using synthetic data may limit generalization, and future applications should validate the approach with real PS seismic data.

A complete validation would require multi-component seismic field data, which was not available for this study. To our knowledge, this type of data has not yet been acquired in our country, and previous attempts to obtain it from other sources have been unsuccessful. In a real-data application, the algorithm should be applied following the same procedure used for the synthetic examples presented here. While parameter values might need to be adjusted, the flexibility of the method facilitates adaptation to different geological and acquisition scenarios. The synthetic cases were designed to be realistic, or at least representative-enough, to provide a reasonable indication of the conditions and challenges likely to be encountered when working with field data.

## CONCLUSIONS

PP-PS data registration often results in non-stationary PS data with artifacts and waveform distortions that can mislead geological interpretation. These issues must be corrected before further processing. Our proposed approach overcomes these limitations by operating in the reflectivity domain instead of the data domain. The method iteratively warps a sparse-spike reflectivity estimated from the PS data until its seismic trace envelope matches the PP counterpart. Reflectivities are computed using  $l_1$ -norm regularization for 1D data or total variation for 2D data, solved with FISTA. The warping function is derived from a  $v_P/v_S$  ratio estimation, parameterized using monotone cubic splines, with optimal knot values determined via VFSA.

Numerical tests confirm that the method effectively produces stationary PP and PS seismic traces with well-aligned reflectors and preserved amplitudes in both 1D and 2D scenarios. The proposed approach outperforms conventional registration techniques, such as DTW, by eliminating waveform distortions, reducing noise, and improving spectral consistency, ensuring more reliable data for further processing and interpretation.

The 2D example, despite relying on synthetic PS data, demonstrated the method's robustness and practical applicability. Future work should validate its performance on actual field PS data and explore adaptive parameter selection and extensions to more complex seismic scenarios.

**Acknowledgments** The authors gratefully acknowledge the continuous support of the Universidad Nacional de La Plata (UNLP), the Consejo Nacional de Investigaciones Científicas y Técnicas (CONICET), and the Agencia Nacional de Promoción de la Investigación, el Desarrollo Tecnológico y la Innovación, Argentina.

## REFERENCES

- Anderson, K. R., & Gaby, J. E. (1983). Dynamic waveform matching. *Information Sciences*, 31(3), 221–242. [https://doi.org/10.1016/0020-0255\(83\)90054-3](https://doi.org/10.1016/0020-0255(83)90054-3)
- Backus, G. E. (1962). Long-wave elastic anisotropy produced by horizontal layering. *Journal of Geophysical Research (1896-1977)*, 67(11), 4427–4440. <https://doi.org/10.1029/JZ067i011p04427>

- Beck, A., & Teboulle, M. (2009). Fast gradient-based algorithms for constrained total variation image denoising and deblurring problems. *IEEE Transactions on Image Processing*, 18(11), 2419–2434. <https://doi.org/10.1109/TIP.2009.2028250>
- Castagna, J., Batzle, M., & Eastwood, R. (1985). Relationships between compressional and shear-wave velocities in clastic silicate rocks. *Geophysics*, 50, 551–570. <https://doi.org/10.1190/1.1441933>
- Chai, X., Tang, G., Lin, K., Yan, Z., Gu, H., Peng, R., Sun, X., & Cao, W. (2021). Deep learning for multitrace sparse-spike deconvolution. *Geophysics*, 86(3), V207–V218. <https://doi.org/10.1190/geo2020-0342.1>
- Chambolle, A. (2004). An algorithm for total variation minimization and applications. *Journal of Mathematical Imaging and Vision*, 20(1), 89–97. <https://doi.org/10.1023/B:JMIV.0000011325.36760.1e>
- Chopra, S., & Sharma, R. K. (2020). Addressing artifacts in PP-PS registration prior to performing joint impedance inversion. *The Leading Edge*, 39(1), 47–52. <https://doi.org/10.1190/tle39010047.1>
- Compton, S., & Hale, D. (2014). Estimating VP/VS ratios using smooth dynamic image warping. *Geophysics*, 79(6), V201–V215. <https://doi.org/10.1190/geo2014-0022.1>
- Cooke, D., & Schneider, W. (1983). Generalized linear inversion of reflection seismic data. *Geophysics*, 46(6), 665–676. <https://doi.org/10.1190/1.1441497>
- Debeye, H. W. J., & van Riel, P. (1990).  $L_p$ -norm deconvolution. *Geophysical Prospecting*, 38(4), 381–403. <https://doi.org/10.1111/j.1365-2478.1990.tb01852.x>
- Fomel, S. (2007). Local seismic attributes. *Geophysics*, 72(3), A29–A33. <https://doi.org/10.1190/1.2437573>
- Fomel, S., & Backus, M. M. (2003). Multicomponent seismic data registration by least squares. *SEG Technical Program Expanded Abstracts*, 781–784. <https://doi.org/10.1190/1.1818052>
- Fomel, S., Backus, M., Fouad, K., Hardage, B., & Winters, G. (2005). A multistep approach to multicomponent seismic image registration with application to a West Texas carbonate reservoir study. *SEG Technical Program Expanded Abstracts*, 1018–1021. <https://doi.org/10.1190/1.2147852>
- Fritsch, F. N., & Butland, J. (1984). A method for constructing local monotone piecewise cubic interpolants. *SIAM Journal on Scientific and Statistical Computing*, 5(2), 300–304. <https://doi.org/10.1137/0905021>
- Gaiser, J. E. (1996). Multicomponent VP/VS correlation analysis. *Geophysics*, 61(4), 1137–1149. <https://doi.org/10.1190/1.1822598>
- Gao, W., & Sacchi, M. D. (2018). Multicomponent seismic data registration by nonlinear optimization. *Geophysics*, 83(1), V1–V10. <https://doi.org/10.1190/geo2017-0105.1>
- Gardner, G., Gardner, L., & Gregory, A. (1974). Formation velocity and density: The diagnostic basics for stratigraphic traps. *Geophysics*, 74, 770–780. <https://doi.org/10.1190/1.1440465>
- Geis, W. T., Stewart, R. R., Jones, M. J., & Katapodis, P. E. (1990). Processing, correlating, and interpreting converted shear waves from borehole data in southern Alberta. *Geophysics*, 55(6), 660–669. <https://doi.org/10.1190/1.1442878>
- Gelpi, G., Pérez, D. O., & Velis, D. R. (2020). Automatic well tying and wavelet phase estimation with no waveform stretching or squeezing. *Geophysics*, 85(3), D83–D91. <https://doi.org/10.1190/geo2019-0284.1>
- Gelpi, G. R., Pérez, D. O., & Velis, D. R. (2019). Seismic wavelet phase estimation by  $l_1$ -norm minimization. *Journal of Seismic Exploration*, 28(4), 393–411. <https://geophysical-press.com/journal/JSE/articles/150>
- Geng, W., Chen, X., Li, J., Wang, J., Wu, F., Tang, W., & Zhang, J. (2023). Warped P-SV wavelet distortion correction using a time-frequency adaptive shaping filter. *Geophyscs*, 88(2), V101–V112. <https://doi.org/10.1190/geo2022-0368.1>
- Hale, D. (2013). Dynamic warping of seismic images. *Geophysics*, 78(2), S105–S115. <https://doi.org/10.1190/geo2012-0327.1>
- Hennenfent, G., van den Berg, E., Friedlander, M. P., & Hermann, F. J. (2008). New insights into one-norm solvers from the Pareto curve. *Geophysics*, 73(4), 23–26. <https://doi.org/10.1190/1.2944169>
- Herrera, H., Fomel, S., & van der Baan, M. (2014). Automatic approaches for seismic to well tying. *Interpretation*, 2(2), SD101–SD109. <https://doi.org/10.1190/INT-2013-0130.1>
- Ingber, L. (1989). Very fast simulated re-annealing. *Journal of Mathematical Computation and Modelling*, 12, 967–973. [https://doi.org/10.1016/0895-7177\(89\)90202-1](https://doi.org/10.1016/0895-7177(89)90202-1)
- Kazemi, N. (2018). Automatic blind deconvolution with Toeplitz-structured sparse total least squares. *Geophysics*, 83(6), V345–V357. <https://doi.org/10.1190/geo2018-0136.1>
- Lindsay, R., & Van Koughnet, R. (2001). Sequential Backus averaging: Upscaling well logs to seismic wavelengths. *The Leading Edge*, 20(2), 188–191. <https://doi.org/10.1190/1.1438908>
- Liner, C. L., & Clapp, R. G. (2004). Nonlinear pairwise alignment of seismic traces. *The Leading Edge*, 23(11), 1146–1150. <https://doi.org/10.1190/1.1825937>
- Lines, L., Zou, Y., Zhang, A., Hall, K., Embleton, J., Palmiere, B., Reine, C., Bessette, P., Cary, P., & Secord, D. (2005). VP/VS characterization of a heavy-oil reservoir. *The Leading Edge*, 24(11), 1134–1136. <https://doi.org/10.1190/1.2135111>

- Lu, J., Yang, Z., Wang, Y., & Shi, Y. (2015). Joint PP and PS AVA seismic inversion using exact Zoeppritz equations. *Geophysics*, 80(5), R239–R250. <https://doi.org/10.1190/geo2014-0490.1>
- Needleman, S. B., & Wunsch, C. D. (1970). A general method applicable to the search for similarities in the amino acid sequence of two proteins. *Journal of Molecular Biology*, 48(3), 443–453. [https://doi.org/10.1016/0022-2836\(70\)90057-4](https://doi.org/10.1016/0022-2836(70)90057-4)
- Oldenburg, D. W., Scheuer, T., & Levy, S. (1983). Recovery of the acoustic impedance from reflection seismograms. *Geophysics*, 48(10), 1318–1337. <https://doi.org/10.1190/1.1441413>
- Pereg, D., Cohen, I., & Vassiliou, A. A. (2020). Sparse seismic deconvolution via recurrent neural network. *Journal of Applied Geophysics*, 175, 103979. <https://doi.org/10.1016/j.jappgeo.2020.103979>
- Pérez, D. O., Velis, D. R., & Sacchi, M. D. (2013). High-resolution prestack seismic inversion using a hybrid FISTA least-squares strategy. *Geophysics*, 78(5), R185–R195. <https://doi.org/10.1190/geo2013-0077.1>
- Pérez, D. O., & Velis, D. R. (2011). Sparse-spike AVO/AVA attributes from prestack data. *SEG Technical Program Expanded Abstracts*, 30, 340–344. <https://doi.org/10.1190/1.3627906>
- Pérez, D. O., & Velis, D. R. (2018). Simple and fast gradient-based impedance inversion using total variation regularization. *Journal of Seismic Exploration*, 27(5), 473–486. <https://geophysical-press.com/journal/JSE/articles/174>
- Pérez, D. O., Velis, D. R., & Sacchi, M. D. (2017). Three-term inversion of prestack seismic data using a weighted  $l_{2,1}$  mixed norm. *Geophysical Prospecting*, 65(6), 1477–1495. <https://doi.org/10.1111/1365-2478.12500>
- Ricker, N. (1940). The form and nature of seismic waves and the structure of seismograms. *Geophysics*, 5, 348–366. <https://doi.org/10.1190/1.1441816>
- Robinson, E. A., & Eberhart-Phillips, D. A. (1996). *Deconvolution 2*. SEG.
- Rudin, L. I., Osher, S., & Fatemi, E. (1992). Nonlinear total variation based noise removal algorithms. *Physica D: Nonlinear Phenomena*, 60(1), 259–268. [https://doi.org/10.1016/0167-2789\(92\)90242-F](https://doi.org/10.1016/0167-2789(92)90242-F)
- Sacchi, M. D. (1997). Reweighting strategies in seismic deconvolution. *Geophysical Journal International*, 129(3), 651–656. <https://doi.org/10.1111/j.1365-246X.1997.tb04500.x>
- Sacchi, M. D., Velis, D. R., & Ulrych, T. J. (1996). Wavelet via polycepstra. *SEG Technical Program Expanded Abstracts*, 1583–1586.
- Sakoe, H., & Chiba, S. (1978). Dynamic programming algorithm optimization for spoken word recognition. *IEEE Transactions on Acoustics, Speech, and Signal Processing*, 26(1), 43–49. <https://doi.org/10.1109/TASSP.1978.1163055>
- Stewart, R. R., Gaiser, J. E., Brown, R. J., & Lawton, D. C. (2003). Converted-wave seismic exploration: Applications. *Geophysics*, 68(1), 40–57. <https://doi.org/10.1190/1.1543193>
- Sui, Y., & Ma, J. (2020). Blind sparse-spike deconvolution with thin layers and structure. *Geophysics*, 85(6), V481–V496. <https://doi.org/10.1190/geo2019-0423.1>
- Taner, M. T., Koehler, F., & Sheriff, R. E. (1979). Complex seismic trace analysis. *Geophysics*, 44(6), 1041–1063. <https://doi.org/10.1190/1.1440994>
- Taylor, H. L., Banks, S. C., & McCoy, J. F. (1979). Deconvolution with the  $l_1$  norm. *Geophysics*, 44(1), 39–52. <https://doi.org/10.1190/1.1440921>
- van den Berg, E., & Friedlander, M. (2008). Probing the Pareto frontier for basis pursuit solutions. *SIAM Journal of Scientific Computing*, 31(2), 890–912. <https://doi.org/10.1137/080714488>
- Walden, A., & Hosken, J. (1986). The nature of the non-Gaussianity of primary reflection coefficients and its significance for deconvolution. *Geophysical Prospecting*, 34, 1038–1066.
- Wiggins, R. (1978). Minimum entropy deconvolution. *Geoexploration*, 16, 21–35. [https://doi.org/10.1016/0016-7142\(78\)90005-4](https://doi.org/10.1016/0016-7142(78)90005-4)
- Yilmaz, Ö. (2001). *Seismic data analysis: Processing, inversion, and interpretation of seismic data*. Society of Exploration Geophysicists. <https://doi.org/10.1190/1.9781560801580>
- Yuan, J. J., Nathan, G., Calvert, A., & Bloor, R. (2008). Automated C-wave registration by simulated annealing. *SEG Technical Program Expanded Abstracts*, 1043–1047. <https://doi.org/10.1190/1.3059105>
- Zhang, F., & Wang, Y. (2009). Amplitude-preserving calibration of PP- and PS-wave reflection events. *SEG Global Meeting Abstracts*, 82–82. <https://doi.org/10.1190/1.3603607>
- Zoeppritz, K. (1919). VII b. über reflexion und durchgang seismischer wellen durch unstetigkeitsflächen. *Nachrichten von der Gesellschaft der Wissenschaften zu Göttingen, Mathematisch-Physikalische Klasse*, 1919, 66–84. <http://eudml.org/doc/59042>
- Zuleta, L. M., & Lawton, D. C. (2012). VP/VS characterization of a shale gas basin, northeast British Columbia, Canada. *SEG Technical Program Expanded Abstracts*, 1–5. <https://doi.org/10.1190/segam2012-1172.1>